The Viscosity of Multiphase Lava: New Insights from Integrating Laboratory and Field Measurements

M A Harris, S Kolzenburg, M O Chevrel

Harris et al. 2025 Author Accepted Manuscript. Earth and Planetary Science Letters
Accepted 12 September 2025: https://doi.org/10.1016/j.epsl.2025.1196

The Viscosity of Multiphase Lava: New Insights from Integrating Laboratory and Field Measurements

M.A. Harris[1,a], S. Kolzenburg[1], and M.O. Chevrel[1,2,3,4]

[1]*Department of Earth Sciences, University at Buffalo, 126 Cooke Hall Buffalo, NY 14260-4130, USA*
[2]*Université Clermont Auvergne, CNRS, IRD, OPGC, Laboratoire Magmas et Volcans, 63000 Clermont-Ferrand, France.*
[3]*Université Paris Cité, Institut de physique du globe de Paris, CNRS, 75005 Paris, France*
[4]*Observatoire volcanologique du Piton de la Fournaise, Institut de physique du globe de Paris, 97418 La Plaine des Cafres, France*

a) Corresponding Author: martin.a.harris95@gmail.com

ABSTRACT

Laboratory measurements on remelted rocks are the standard technique for characterizing the rheology of lava at eruptive temperatures. This approach enables precise measurements but struggles to recreate natural emplacement conditions. Particularly, lavas erupt as multiphase suspensions (melt + crystals + bubbles), but current laboratory methods cannot retain bubbles, and experiments are limited to two-phase (melt+crystals) suspensions. The oxygen fugacity of lavas is known to influence the kinetics of crystallization, and despite its importance, few studies have considered this factor to date. The only available technique to measure the three-phase viscosity of natural lava is through *in-situ* measurements while it is flowing. Here, we present the first study that integrates viscosity data from laboratory-derived single (melt) and two-phase (melt+crystals) measurements with data from three-phase (melt + crystals + bubbles) field measurements, using the 2023 Litli-Hrútur eruption in Iceland as a case study. We present a rheological characterization of the remelted lava during crystallization at thermomechanical equilibrium and disequilibrium at log fO_2 = −8.7, and deformation rates of 3.3 s^{-1}. These bubble-free laboratory experiments were designed to overlap with field temperatures (1150-1165 ℃), enabling direct comparison with the *in-situ* three-phase field viscosities. We find laboratory and field data overlap in viscosity space ($10^{2.5}$ to $10^{4.5}$ Pa s) and at cooling rates of 0.5-1 ℃/min. Isothermal experiments successfully recreate crystal phases and volumes comparable to natural samples (~20-50 vol.% crystals). This comparison allows the first field validation for laboratory measurements of the effective viscosity of natural lava.

1 Introduction

The viscosity of magma and lava influences volcanic eruptive style and flow trajectory, velocity, and runouts. Understanding lava viscosity can help refine numerical models and emergency response procedures (Chevrel et al., 2022; Hyman et al., 2024). Studies of lava viscosity predominantly use laboratory experiments (see review by Kolzenburg et al., 2022). Although these experiments enable precise control of temperature, shear rate, and oxygen fugacity (fO_2), the latter has seldom been used to match experimental to natural conditions. It is known that fO_2 influences melt viscosity (Dingwell and Virgo, 1987; Chevrel et al., 2013), and, at sub-liquidus conditions, it affects both crystallization kinetics and the crystal volume fraction, thereby varying the effective viscosity. Natural lavas erupt at log fO_2 = -8 to -11 and are reduced compared to atmospheric conditions (log fO_2 = -0.68 at 1200°C) (Hamilton et al., 1964; Sato, 1978; Markl et al., 2010; Mollo et al., 2015; Kolzenburg et al., 2018a). For basalts, this reduced state tends to: 1) reduce the melt viscosity because it reduces Fe^{3+} to Fe^{2+}, changing melt structure; and 2) shift the onset of crystallization, causing the lavas to reach lower temperatures before crystallization induces viscosity increases (Di Genova et al., 2017; Kolzenburg et al., 2018a). This means laboratory measurements performed in air are not representative of eruptive conditions, and delineate the high-temperature limit of rheological changes (Kolzenburg et al., 2018a).

Natural lavas are multiphase, containing melt, crystals, and bubbles. However, standard laboratory measurements for low-viscosity lavas (Si-poor) allow bubbles to escape during remelting, leaving only melt and melt+crystals suspensions accessible for stable and reproducible experimentation. There have been efforts to parameterize three-phase suspensions through combining two-phase models of viscosity via the effective medium

Harris et al. 2025 Author Accepted Manuscript. Earth and Planetary Science Letters
Accepted 12 September 2025: https://doi.org/10.1016/j.epsl.2025.1196

theory (Phan-Thien and Pham, 1997). Recent analog studies have considered three-phase suspensions (Truby et al., 2015; Birnbaum et al., 2021). But these experiments, while spanning a wide range of bubble and crystal fractions ($0 \leq 0.82$ and $0 \leq 0.5$, respectively), lack the polydispersity of bubbles and crystals, and the large, deformable bubbles present in natural lavas (i.e., Fig. 1).

Recently, Halverson and Whittington (2024) attempted to retain the bubbles during concentric cylinder viscosity measurements on partially molten lava by rapidly melting and simultaneously measuring viscosity before complete bubble escape. This method shows promise for measuring three-phase lava; however, the experiments require rapid temperature changes that induce extreme disequilibrium conditions with little control over phase proportions or thermal homogeneity. The progression of an increase in crystallization with a decrease in vesicularity from vent to flow front observed in natural lavas (Cashman et al., 1999; Robert et al., 2014; Harris et al., 2024a) is difficult to replicate with such experiments. Measuring natural lava viscosity via *in-situ* field viscometry is the most promising method for characterizing three-phase lava viscosity with naturally progressing suspended phase proportions of crystals and bubbles (Chevrel et al., 2018a, 2019; Harris et al., 2024a). *In-situ* viscometry is challenging due to dynamic and hazardous field conditions, but recent advances in field viscometer design have provided more portable and precise instruments that can enable rapid, safe, and accurate collection of viscosity data on active lavas (Chevrel et al., 2023; Harris et al., 2024a,b).

Here we present the first comprehensive study that integrates field measurements of lava during the 2023 Litli-Hrútur (LH) eruption in Iceland performed by Harris et al. (2024a) with single- and two-phase viscosity data obtained through laboratory experimentation under controlled fO_2. The laboratory experimental data overlap the field data in temperature, crystallinity, and viscosity space. This enables us to evaluate the magnitude of the effects that various proportions of crystals and bubbles have on the viscosity of three-phase natural lava. We investigate how well commonly used model-derived viscosities reproduce the field viscosities. Given that the modeling of multiphase lavas is a critical component of active volcanic hazard response (Harris et al., 2019; Pedersen et al., 2023; Hyman et al., 2024), this comprehensive comparison serves as a milestone for future work that aims to improve the prediction and treatment of suspended phases within lavas.

2 Methods

2.1 Experimental Materials and Methods

Samples were collected from lava during the 2023 LH eruption, Reykjanes Peninsula, Iceland (Fig. 1; Harris et al., 2024a). The lava's groundmass crystallinity increased from ~25% to ~50% and vesicularity decreased from 32% to 2% along the 3.5 km long flow. Plagioclase was the only major mineral phase, with minor olivine and Ca-pyroxene. The location of the sample used here was Site 4, ~900 m down channel from the vent (Fig. 1C). Lava was collected and quenched using a metal scoop. The sample contained 33 vol.% groundmass crystals and 12 vol.% bubbles, with an average crystal aspect ratio of 2.5 (Harris et al., 2024a).

The sample was powdered and melted at 1350˚C in air using a Carbolite Gero HTF 1700 furnace in the Laboratory for Experimental Volcanology and Petrology at the University at Buffalo (LAVAP-UB). We used a Fe-saturated 100 ml platinum (Pt) crucible that was filled incrementally (~10 grams every 5 minutes). Once filled, the melt was left at the temperature for 30 minutes to ensure complete melting of all phases and then quenched to a glass in a copper box. This glass was crushed and remelted to ensure sample homogeneity.

The glass was remelted into a cylindrical crucible $Pt_{90}Ir_{10}$, 51 mm in height, and 26.6 mm in diameter, used for concentric cylinder viscometry. Once filled, it was loaded into a Micropyretics Heaters International (MHI) 1400 vertical split-tube furnace. An Anton Paar DSR 502 rheometer was fixed above the furnace, and a cylindrical aluminum oxide spindle capped with a Pt sheath (5.2 mm outer diameter) was immersed (~ 40 mm) into the melt. These measurements record the torque exerted by the melt onto the spindle that rotates at a constant speed (*i.e.,* shear rate). Viscosity measurements were calibrated using a DGG-1 standard glass from the German Glass Society, and data were processed following the approach of Kolzenburg et al. (2016). Sample temperature was calibrated using a type S thermocouple immersed in a DGG-1 melt for constant temperature steps and for each cooling rate to account for thermal lag of the sample.

Experiments were performed in an fO_2-controlled atmosphere under a constant CO/CO_2 gas mixture at a 40/60 ratio and a volumetric flux of 400 ml/min (*e.g.,* Deines et al., 1976; Kolzenburg et al., 2018). The melt was equilibrated under these conditions at 1350℃ and stirred at a shear rate of 6.6 s^{-1} (*i.e.,* 30 rotations per minute (rpm)), for 24 hours before measurements started. This places the melt at $\log fO_2 = -8.7$, similar to typical Icelandic basalts at shallow crustal depths (~$\log fO_2$ = -8.9 to -7.1; Willhite et al., 2024).

Melt viscosity was measured at super liquidus conditions and is reported in increments of 20℃ from 1290℃ to 1190℃. Shear rate steps from 0.02-10.9 s^{-1} (0.1 to 50 rpm) were applied to verify the Newtonian character of the melt, confirming that no crystallization had occurred.

Harris et al. 2025 Author Accepted Manuscript. Earth and Planetary Science Letters
Accepted 12 September 2025: https://doi.org/10.1016/j.epsl.2025.1196

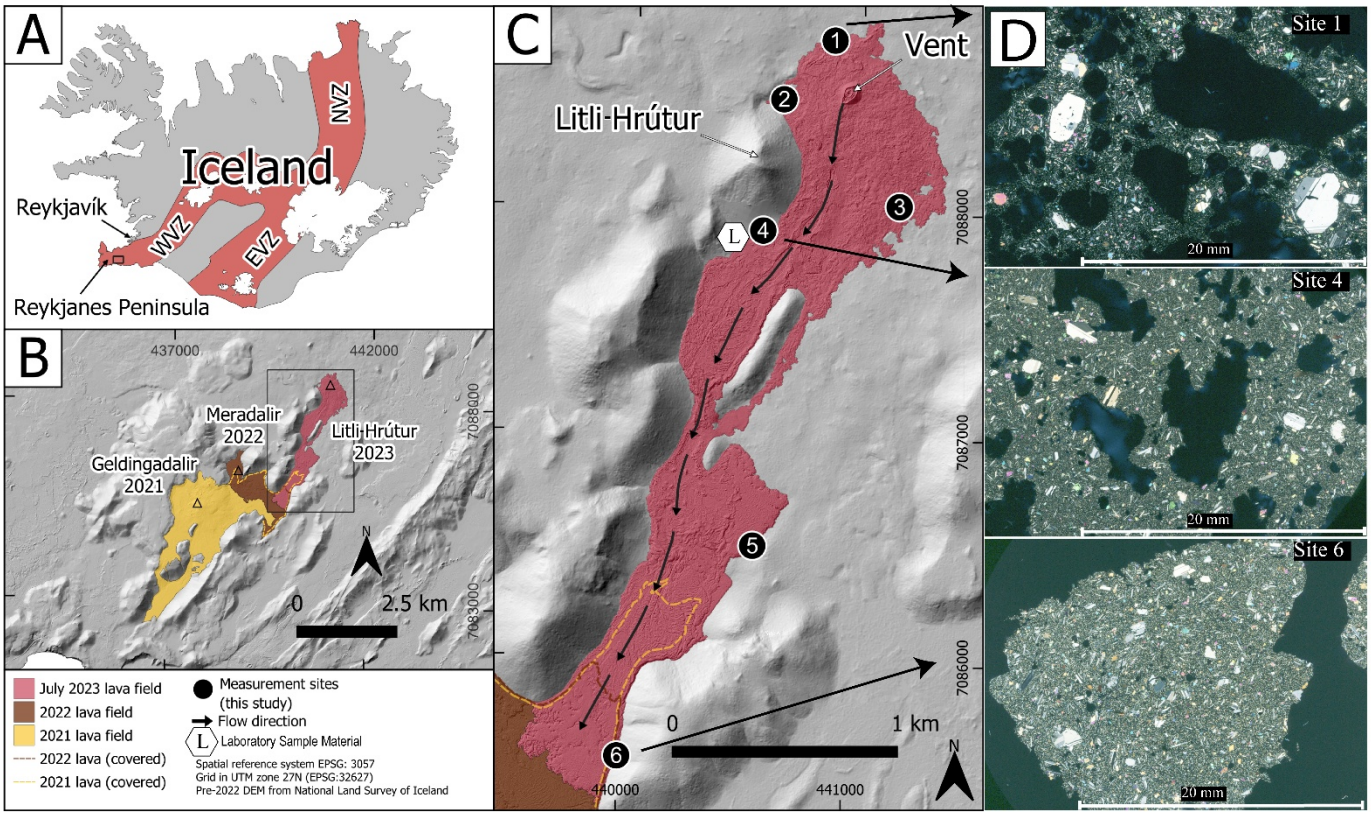

Figure 1: *Geologic map modified from Harris et al. (2024a) showing the location of the Litli-Hrútur lava field, Iceland. A) Regional setting of the eruption site within the southwest Reykjanes Peninsula. The black rectangle denotes the submap B location. Rift zones (red) and ice caps (white) are shown. B) Map showing the extent of the 2021, 2022, and 2023 lava flow fields in the area. Triangles denote approximate vent locations. The black rectangle denotes the submap C extent. C) Map showing the extent of the lava flow field with the six measurement site locations of Harris et al. (2024a) and the location of the sample at site 4 used here for experimentation (L). D) Representative cross-polarized petrographic images of natural, three-phase Litli-Hrútur lavas.*

Sub-liquidus suspension viscosities at thermomechanical equilibrium (hereafter called isothermal deformation experiments (IDE) after Di Fiore et al., 2021) were measured by imposing a constant shear rate above the liquidus for at least 2 hours to ensure complete melting of crystal phases and then cooling to target subliquidus temperatures (1200, 1190, 1180, 1175, 1165, and 1155℃) at a rate of 10 °C/min, holding for ~8-10 hours until thermomechanical equilibration was achieved (*i.e.*, constant torque and apparent viscosity) (Vona et al., 2011), ensuring thermal equilibrium and homogenous crystal distribution across the crucible (Chevrel et. al. 2015). The shear rate was held constant for each IDE, at 3.3 s^{-1} (15 rpm), as variations in shear rates affect the crystallization kinetics of lavas (Kolzenburg et al., 2018b). The sample's apparent viscosity was determined by averaging the data from the last hour of measurement for each IDE plateau. After an IDE was completed, the spindle and crucible were dropped together from the furnace and water quenched to preserve syn-experimental textures (Chevrel et al., 2015; Fig. S1.1). The alumina rod, Pt sheath, and partially crystallized sample were extracted from the crucible using a diamond-tipped core drill and prepared for textural quantification.

Viscometry under constant cooling (hereafter called cooling deformation experiments: CDE after Di Fiore et al., 2021) was performed to simulate conditions that lavas undergo as they erupt and cool until their rheological threshold is reached and the lava solidifies (Kolzenburg et al., 2017, 2019, 2020). Typical cooling rates for basaltic lavas are in the range of 0.1 to 10 °C/min (Kolzenburg et al., 2016 and references therein). We used 0.25, 0.5, 1, and 3 °C/min for the experiments performed for this study. The upper cooling rate limit of 3 °C/min ensured thermal homogeneity within the sample since higher cooling rates impose thermal gradients in the crucible, inhibiting meaningful interpretation of derived viscosity data (Kolzenburg et al., 2016). For these experiments, the initial shear rates and rotational speeds were set to match those of the IDE (3.3 s^{-1} and 15 rpm, respectively). During cooling, the viscosity increased initially due to the temperature dependence of the melt. Once crystallization commenced,

Harris et al. 2025 Author Accepted Manuscript. Earth and Planetary Science Letters
Accepted 12 September 2025: https://doi.org/10.1016/j.epsl.2025.1196

the increase in viscosity accelerated significantly. Every time the measurement reached a set torque limit of 15 mNm, the imposed shear rate was reduced by 20% to enable continued viscosity measurements. A cooling sequence was completed when the torque limit was reached at a shear rate of 0.0002 s^{-1} (0.001 rpm). At the end of a cooling sequence, the sample was returned to 1350°C for ~2 hours to allow for re-melting of all crystals and thermal homogenization. This was confirmed by recovering the melt viscosity of crystal-free measurements, following the approach detailed in Kolzenburg et al. (2018a). Crystallization is too rapid in low-viscosity melts to preserve the texture of CDE samples during quench.

After completion of CDEs, the crucible containing the reduced and re-equilibrated melt at super-liquidus conditions was removed from the furnace, and the melt was quenched in a copper box. Pieces of this reduced glass were cut and polished for micropenetration viscometry near the glass transition temperature (Tg). This procedure pushes a small ceramic bead into the sample under constant force and measures the resulting indentation rate (Hess and Dingwell, 1996; Vona et al., 2017; Webb, 2021). Measurements were conducted at 710℃ and 750℃. Nanolite crystallization may occur during micropenetration of basalts, which may cause viscosity increases near Tg (Fanesi et al., 2025). As the data only serve here as pinpoints for generating the temperature-dependent non-Arrhenian Vogel-Fulcher-Tammann (VFT) (Vogel, 1921; Fulcher, 1925) viscosity model for crystal-free melt, any nanocrystallization would result in variations at high temperature that are below the reported uncertainties. A fragment of this glass was also chemically analyzed (see sections 2.3 and 2.4).

2.2 Field Viscometry

The viscosity of LH lava was measured *in-situ* along the length of the flow field by Harris et al. (2024a). For low viscosities (<10^3 Pa s), a motor-driven rotational viscometer (RV) presented in Chevrel et al. (2023) was used, which records the torque of a rotating shear vane immersed in the lava for one to three minutes. For higher viscosity (10^3-10^5 Pa s), the axial viscometer (penetrometer-type (LP)) presented in Harris et al. (2024b) was used, which records the force required to push a hemispherical indenter into the lava for ~20 cm over ~2-15 seconds. Along with field viscometry, the lava thermal evolution was documented by *in-situ* measurements using K-type thermocouples. Two to three thin sections of natural lava were analyzed using scanning electron microscopy (SEM) from each site to capture the textural heterogeneity of the lava (Harris et al., 2024a). Whole-rock geochemical analyses of LH lava are reported in Table S2.1.

2.3 Textural and Geochemical Analysis of Experimental Samples

Thin sections from the upper and lower portions of the crucible were analyzed for each IDE. Optical, SEM, and energy dispersive X-ray spectroscopy (EDS) were carried out at the University at Buffalo shared facilities center (Hitachi S4000). Ten to fourteen SEM images ranging from 70x to 500x magnification of the thin sections were converted to gray-scale, cleaned of cracks and non-groundmass cargo with Photoshop®, and then processed with ImageJ (*e.g.,* Schneider et al., 2012) to determine crystal area fraction. A similar method was used to estimate the bubble fraction within the natural lava samples using two to three full thin-section scans (~25 x 40 mm) for each site (*c.f.,* Harris et al., 2024a). Select area fractions derived from ImageJ (2-dimensional) were processed using the crystal-size-distribution (CSD) program by Higgins (2000) that corrects the 2D thin-section for 3-dimensional analyses. The deviations of values from CSD compared to the direct ImageJ analyses were less than the uncertainties from sample suite heterogeneity. This agreement between 2D and 3D processing indicates that, within uncertainty, the area fractions determined through ImageJ can be treated as equivalent to the volume fraction (Φ) of each sample and are considered as such in this study. All reported crystal abundances refer to the bubble-free crystal content (*i.e.,* crystal fraction of the groundmass excluding the large plagioclase phenocrysts and bubbles) (< 200μm) and are hereafter referred to as Φ_c.

The composition of the glassy matrix of each IDE sample was measured at the Laboratoire Magmas and Volcans on polished thin sections via electron microprobe CAMECA SX 100 (at 15 kV and a defocused beam of 20 μm at a current of 8 nA), and they are reported as averaged values of at least 10 analyses in Table S2.2. A piece of the reduced glass produced in the laboratory (~30 g) was analyzed at ALS Geochemistry Ltd for major element chemistry using X-ray fluorescence. The ferrous iron (Fe^{2+}) content was analyzed by ALS Geochemistry Ltd (Table S2.1) using potassium dichromate titration of the natural lava sample homogenized powder and the reduced glass sample produced in the laboratory.

3 Results

3.1 Laboratory measurements of Litli-Hrútur lava

3.1.2 Liquid Viscosity

The melt viscosity was measured from $10^{0.96}$ Pa s at 1290°C to $10^{1.57}$ Pa s at 1190°C (Figure 2A). A lower temperature could not be reached due to the onset of crystallization before thermal homogenization. Near Tg, we

Harris et al. 2025 Author Accepted Manuscript. Earth and Planetary Science Letters
Accepted 12 September 2025: https://doi.org/10.1016/j.epsl.2025.1196

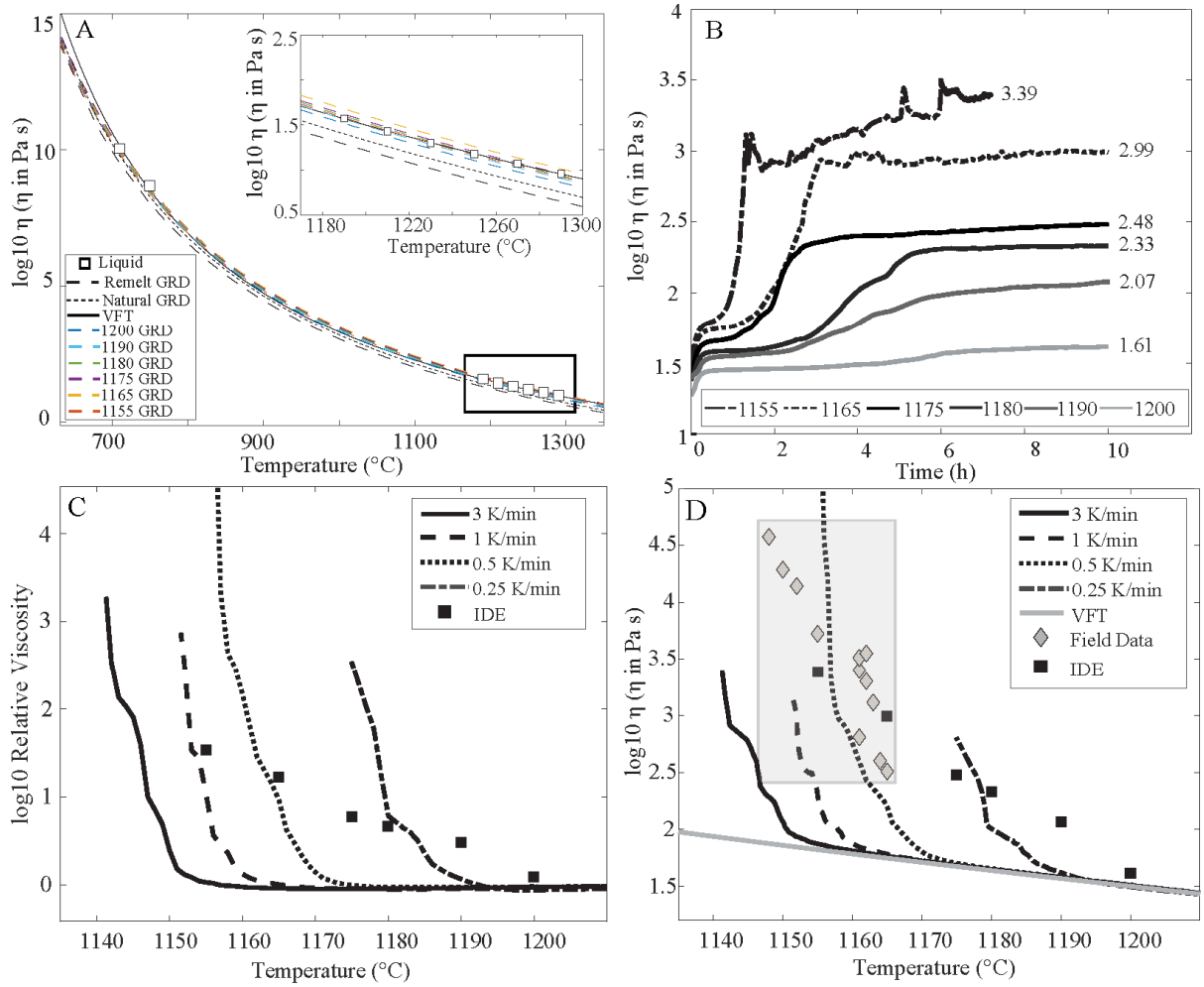

Figure 2: *Laboratory measurements of Litli-Hrútur lava viscosities. A) Measured liquid viscosity data (square boxes) fit with a VFT curve (black line), and GRD models (dashed-black lines), compared to modeled GRD-derived liquid viscosities using the composition of the six glasses from IDE quenched samples at temperatures 1200-1155°C (colored-dash lines). B) Temporal evolution of viscosity during IDEs. Numbers show average viscosities in log Pa s derived from the last hour of measurement of each respective experiment. C) Evolution of relative viscosity in log scale as a function of temperature (°C), where lines represent CDE results at varying cooling rates (0.25 – 3 °C/min) and black squares are IDE average viscosities. D) Integration of all measurements, including liquid viscosity (VFT fit, grey line), the apparent viscosity of the CDE at varying cooling rates, IDE (black square), and field viscosity (grey diamond). Note that the grey field marks the region of overlap for field and laboratory data.*

measured $10^{8.70}$ Pa s at 750°C and $10^{10.05}$ Pa s at 710 °C. We obtained the VFT fit parameters with a fixed A = -4.55 Pa s, fitted B = 5134.07 kJ/mol, and C = 626.88 K. We used a fixed A approach, as it best represents the theoretical high-temperature limit, as detailed in Russell et al. (2003). For comparison, we also plot the Giordano-Russell-Dingwell (GRD) liquid viscosity model (Giordano et al., 2008) calculated from the composition of the natural whole-rock material and the remelted reduced glass (see Supplement 2), which fits reasonably well with our VFT fit but yields a slight underestimation, particularly at higher temperatures (Fig. 2A). Additionally, Figure 2A shows GRD liquid viscosity curves calculated for each IDE glass composition to assess whether the changing crystallinity alters the liquid viscosity, and we find that the slight changes in melt composition (resulting from varying degrees of crystallization) have a negligible effect on viscosity. This is likely also the case for the CDE experiments, as shown previously by Kolzenburg et al. (2017).

3.1.3 Isothermal and Constant Cooling Deformation Experiments

Figure 2B shows the temporal evolution of apparent viscosity for IDE at 1200, 1190, 1180, 1175, 1165, and 1155℃. All experiments followed a characteristic

Harris et al. 2025 Author Accepted Manuscript. Earth and Planetary Science Letters
Accepted 12 September 2025: https://doi.org/10.1016/j.epsl.2025.1196

Table 1: Summary of absolute viscosity measurements of all experiments. For simplicity, interpolated values of the experimental data at equal temperature steps are reported except the final data point for each experiment; highlighted in grey. Temperatures related to those points are reported in the last two rows in Kelvin and Celsius, respectively.

Shear Rate					
Cooling Rate		0.25 K/min	0.5 K/min	1 K/min	3 K/min
Temperature (K)	Temperature (C)	Absolute log10 Viscosity (in Pa s)			
1563	1290	0.96	0.96	0.96	0.99
1558	1285	0.99	0.99	0.99	1.01
1553	1280	1.02	1.02	1.01	1.03
1548	1275	1.05	1.05	1.04	1.05
1543	1270	1.08	1.08	1.07	1.08
1538	1265	1.11	1.11	1.10	1.11
1533	1260	1.14	1.14	1.13	1.13
1528	1255	1.16	1.17	1.16	1.16
1523	1250	1.19	1.19	1.18	1.19
1518	1245	1.22	1.22	1.21	1.22
1513	1240	1.25	1.25	1.24	1.25
1508	1235	1.28	1.28	1.27	1.28
1503	1230	1.31	1.31	1.30	1.31
1498	1225	1.34	1.34	1.34	1.34
1493	1220	1.37	1.37	1.37	1.38
1488	1215	1.40	1.41	1.40	1.41
1483	1210	1.43	1.44	1.43	1.44
1478	1205	1.46	1.47	1.47	1.47
1473	1200	1.49	1.51	1.50	1.51
1468	1195	1.54	1.55	1.54	1.54
1463	1190	1.62	1.58	1.57	1.58
1458	1185	1.78	1.62	1.61	1.61
1453	1180	2.00	1.65	1.64	1.65
1448	1175	2.80	1.70	1.68	1.68
1443	1170		1.80	1.73	1.72
1438	1165		2.20	1.78	1.76
1433	1160		2.78	1.87	1.81
1428	1155		7.57	2.31	1.87
1423	1150		9.16	3.13	2.07
1418	1145				2.77
1413	1140				3.39
T Final Datapoint	K	1448	1427	1425	1414
	C	1175	1154	1152	1141

Harris et al. 2025 Author Accepted Manuscript. Earth and Planetary Science Letters
Accepted 12 September 2025: https://doi.org/10.1016/j.epsl.2025.1196

progression of thermal homogenization of the melt marked by a rapid increase in viscosity, and an incubation period where the viscosity plateaued at the set conditions (Vona et al., 2011; Chevrel et al., 2015; Di Fiore et al., 2021). Following incubation, the onset of crystallization was documented by a gradual increase in viscosity until a second viscosity plateau formed, indicating that a stable crystal content was reached within the sample, and the crystals had arranged in a dynamic textural equilibrium. The incubation time systematically decreased with decreasing experimental temperature (*i.e.,* increased undercooling). Similarly, the crystallization rates (represented as the slope in viscosity-time space) increased with decreasing temperature (increasing undercooling). All measurements, except at 1155°C, ran for ~10 hours until viscosity was stable. At 1155 ℃, the stable viscosity plateau had greater fluctuations than the other experiments. These fluctuations resulted from occasional spindle detachment and reattachment to the partially crystallized sample (Fig. S1.1). This was because the partially crystallized sample was approaching the pāhoehoe-'a'ā transition, where shear can induce viscous rupture (Di Fiore et al., 2021). As a result, the experiment was terminated after ~8 hours following a ~2 hr window of stable readings. This derived apparent viscosity represents a minimum value at the given temperature and stable crystal content due to the potential detachment of the spindle from the melt. IDE apparent viscosities are plotted as individual points in temperature space (Fig. 2C, D). The apparent viscosity increased across the 45 ℃ experimentation from $10^{1.61}$ to $10^{3.39}$ Pa s at 1190 to 1155 °C (Fig. 2B).

In CDE, we observed that the viscosity increased from the pure liquid profile as crystallization began in the temperature range of ~ 1150 to 1195 ℃, depending on the cooling rate (Fig. 2C, D; Table 1). We find that higher cooling rates (1 and 3 °C/min) caused the sample to follow the liquid viscosity curve to lower temperatures (~1160-1150°C) than lower cooling rates (0.25 and 0.5 °C/min; ~1195-1170°C) before crystallization dominated the viscosity changes. This was a result of longer experimental timescales at lower cooling rates, placing the melt in less undercooling, as highlighted in Kolzenburg et al. (2016, 2017, 2018b, 2019). Additionally, the viscosities measured during the higher cooling rate CDE (0.5 – 3 °C/min) were lower than the apparent viscosities from the IDE at overlapping temperatures. The maximum high-threshold viscosity limit for the CDEs at lower cooling rates (0.25 and 0.5 °C/min) reached higher apparent viscosities than the IDE (see discussion below).

We assessed the effect of crystals on the viscosity by calculating the relative viscosity of the two-phase suspension by normalizing the measured viscosity values to the crystal-free liquid viscosity model (VFT fit reported above). This is done for the final stable apparent viscosities of IDE and for the CDE data (Fig. 2C). The IDE relative viscosities echo the stark increase in viscosity with the same ~2 orders of magnitude increase (Fig. 2B), confirming that the viscosity change is directly related to changes in the abundance, size, shape, and distribution of crystals rather than temperature and chemical effects on the viscosity of the interstitial melt (see discussion below).

3.2 Textural characteristics of experimental samples

The post-experimental textures of the IDE samples revealed an increase in crystallinity as temperature decreased (Figs. 3, 4; Table 2). Phase proportions and field temperatures from the natural samples given by Harris et al. (2024a) are reported in Table 2.

Samples from the IDE showed plagioclase as the dominant phase. Between 1200 and 1180 °C, only minor olivine (1 to 5%) was present (Fig. 3A, B, C). Then from 1175 to 1155 °C, Ca-clinopyroxene (3–10%) appeared alongside olivine (3–8%) and plagioclase (20 to 35% (Fig. 3D, F). Minor (<1%) iron oxide was found in all samples. The crystal habits of plagioclase in all samples showed sub-to-euhedral shapes, with typical aspect ratios between 2.5 and 4. Olivine crystals showed subhedral, equant shape. Ca-clinopyroxene crystals were equant with anhedral to subhedral habits.

The phase assemblages of the two lowest temperature IDEs (1165 and 1155 ℃) were consistent with the mineralogy from field samples (Harris et al., 2024a), and they overlapped in phase abundances (Figs. 3G, H, 4A; Table 2).

4 Discussion

4.1 Effect of Crystals on Lava Viscosity

We find that the CDE viscosities can extend to higher values than the IDE viscosities (Figs. 2C, D). This contradicts previous studies that suggested IDEs are the upper limit of viscosity in experimental systems (*c.f.,* Di Fiore et al., 2021, 2023, 2024). We attribute the extent of higher values to a result of variations in crystal habit between the respective experiments, and because the concentric cylinder viscometer used in this study is capable of reaching higher torques than those used in prior studies. During IDE, crystals have the time to grow euhedral shapes, whereas during the CDEs, the crystal growth is more rapid, and therefore skeletal, and acicular-shaped crystals form preferentially (Kolzenburg et al., 2018a). It has been shown through analog studies that the effective viscosity of suspensions is sensitive to increasing aspect ratios and particle roughness due to their effect on the maximum packing fraction and the onset of particle-particle interactions (Mader et al., 2013; Moitra and Gonnermann, 2015; Klein et al., 2017). We interpret that euhedral crystals forming during the IDEs induce a lower effective viscosity than those, more acicular, growing in disequilibrium in the

Harris et al. 2025 Author Accepted Manuscript. Earth and Planetary Science Letters
Accepted 12 September 2025: https://doi.org/10.1016/j.epsl.2025.1196

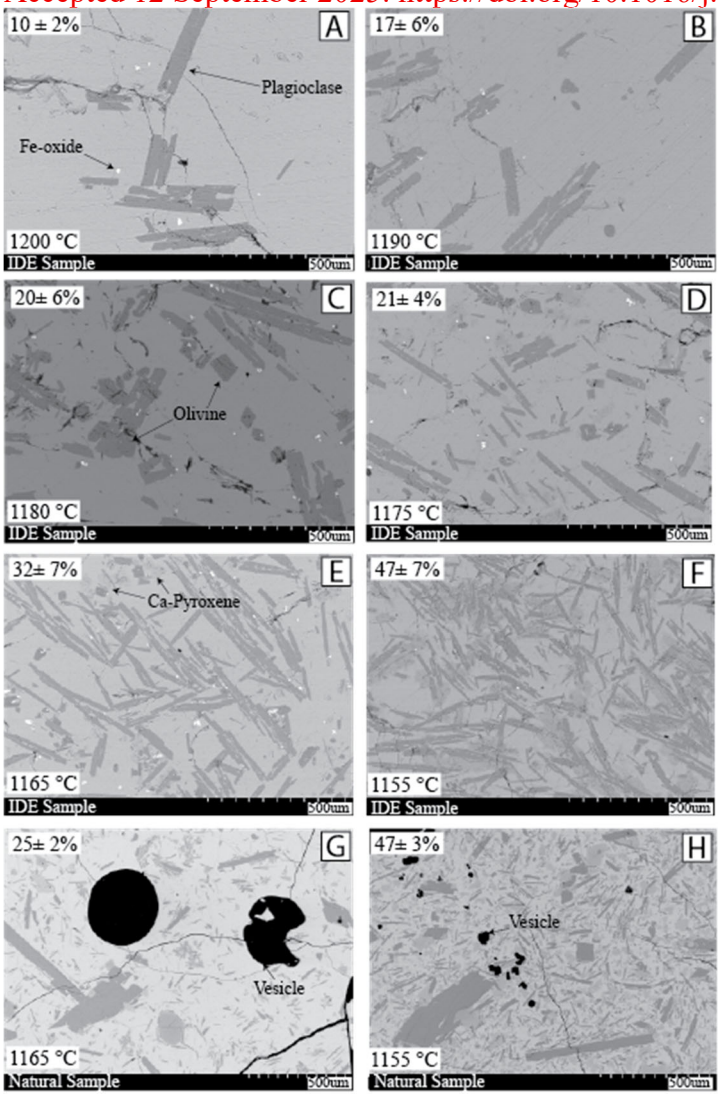

Figure 3: *Representative SEM photomicrographs for each quenched sample from IDEs (A-F), showing backscatter imagery of crystallization. G and H represent natural Litli-Hrútur lavas collected at 1165 and 1155 ℃, respectively (see Harris et al., 2024a for details). Crystal area fractions (bubble-free in G and H) for each sample and their uncertainties derived from analyzing multiple images (see methods for details) are reported in the top left corner of each image.*

CDEs. Additionally, the skeletal growth of dendritic crystals at concentrated volumes induces the transition from Newtonian to non-Newtonian behavior. This is due to melt being trapped within skeletal portions of acicular crystal habits, at micro- (Arzilli et al., 2022) and nano-scale (Bamber et al., 2025), and becoming effectively immobilized. This results in higher effective solid contents within the suspension during disequilibrium growth than euhedral growth. During magmatic transport at thermal disequilibrium (e.g., in conduits, dikes, and lavas), the skeletal crystals will cause viscosity increases well beyond that of equivalent euhedral crystal volume fractions, resulting in rheologic lockup and/or fragmentation (e.g., Arzilli et al., 2019).

We further investigate how commonly used empirical models can recover the measured two-phase viscosities (IDE). Particularly, we use the ones that account for detailed textural parameters such as the models found in Klein et al. (2018), Frontoni et al. (2022), and Moitra and Gonnermann (2015) (Fig. 5, Table S3.1). We consider the bubble-free crystal fractions (Φ_c) and mean aspect ratios from the textures of IDEs (Table 2). The Klein et al. (2018) model employs a modified Maron and Pierce (1956) equation and incorporates particle aspect ratio and polydispersity to determine the maximum packing fraction (Φ_{max}). The upper and lower boundaries of the relative viscosity obtained from this model (Fig. 5) are determined from the Φ_c uncertainties that propagate into different Φ_{max} ranges. The Frontoni et al. (2022) model utilizes the Costa et al. (2009) approach optimized for the range of particle aspect ratios. Following the IDE samples texture, we bound the relative viscosity range with particle aspect ratios of 2 and 4 (using fit parameters of $\varepsilon = 2.74 \times 10^{-4}$, $\gamma = 3.30$, and $\delta = 13 - \gamma$, and $\varepsilon = 1.0 \times 10^{-6}$, $\gamma = 1.38$, and $\delta = 13 - \gamma$, respectively). We employ the Moitra and Gonnermann (2015) model using their textural parameters for suspension shapes *se* and *e,* comparable to the IDE textures range, as upper and lower bounds.

We find that none of these two-phase models for particle suspensions adequately recover our full IDE data (Fig. 5). Models of Frontoni et al. (2022) and Moitra and Gonnermann (2015) overlap with the IDE data in the dilute crystal regime ($\Phi_c < 40\%$) but do not fully capture the trend with increasing crystal fraction. The model of Klein et al. (2018) underestimates the viscosity for the dilute crystal regime but performs better in the concentrated regime ($\Phi_c \geq 40\%$). These models rely on a characteristic maximum particle packing fraction, Φ_{max} or $\Phi_{critical,}$ that predicts a rapid viscosity increase and delineates the transition to creep flow when reached (see review by Kolzenburg et al., 2022). Although some empirical models account for this rheological transition at high Φ_c using a sigmoidal shape function (Lejeune and Richet, 1995; Costa et al., 2009; Frontoni et al., 2022), our data suggest that the onset of this transition in flow behavior can occur at lower relative viscosities and/or lower crystal fraction than what current models predict for the crystal aspect ratios (Table 2; Fig. 5). This overestimation of relative viscosity from empirical approaches compared with measured relative viscosities from IDEs has also been observed by Giuliani et al. (2025). It is likely a result of the empirical models' breakdown at the onset of non-Newtonian behavior beyond the dilute particle regime ($\Phi_c > 40\%$) and remains unresolved for lavas.

Harris et al. 2025 Author Accepted Manuscript. Earth and Planetary Science Letters
Accepted 12 September 2025: https://doi.org/10.1016/j.epsl.2025.1196

Table 2: Summary of two-phase (IDE) and three-phase (field) temperature, viscosity, and textural data for Litli-Hrútur lavas. Φ_c refers to the bubble-free groundmass crystallinity, and Φ_b is vesicularity.

IDE Data	Temperature ˚C	Log10 η (η in Pa s)	Φc	Φc Uncertainty	Crystal Aspect Ratio	Crystal Aspect Ratio Uncertainty	Φb	Φb Uncertainty
	1200	1.61	0.1	0.02	2.2	1	-	-
	1190	2.07	0.17	0.06	2.4	1	-	-
	1180	2.33	0.2	0.06	2.5	1.1	-	-
	1175	2.47	0.21	0.04	2.4	1.1	-	-
	1165	2.99	0.32	0.07	2.6	1.4	-	-
	1155	3.38	0.47	0.07	2.1	1.1	-	-
Field Data								
	1165	2.51	0.25	0.02	2.5	0.1	0.32	0.05
	1164	2.6	0.3	0.02	2.3	0.1	0.15	0.05
	1161	2.81	0.27	0.04	2.1	0.5	0.19	0.08
	1163	3.11	0.33	0.03	2.4	0.3	0.4	0.06
	1155	3.73	0.47	0.02	2.2	0.2	0.12	0.06
	1150	4.29	0.51	0.01	2	0.2	0.01	0.02

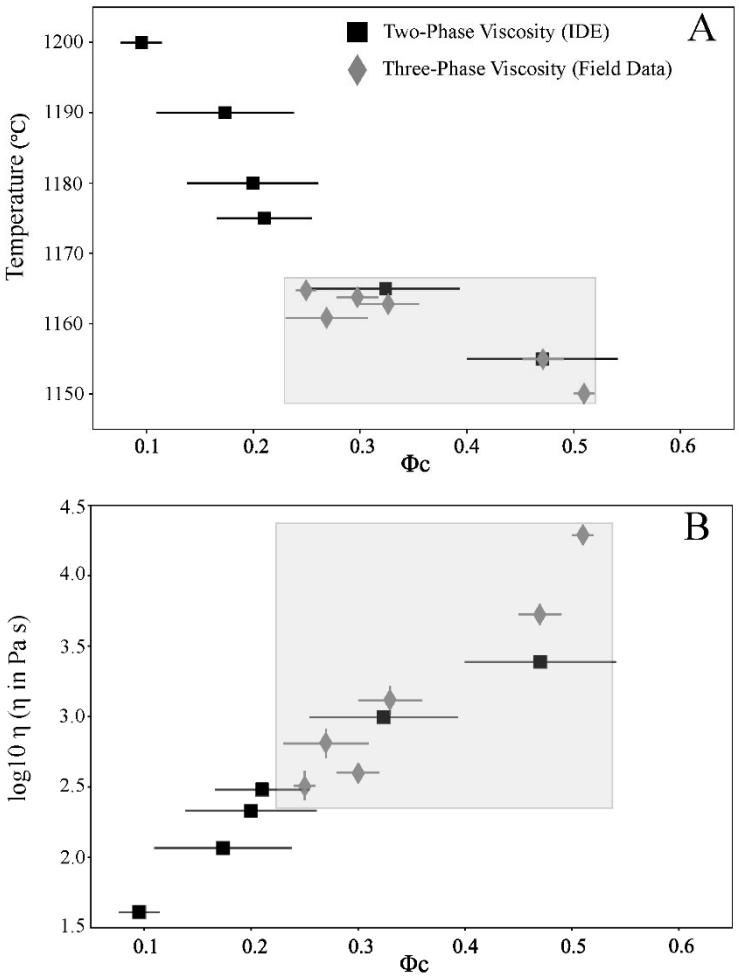

Figure 4: *(A) Two-phase (IDE) (black square) and three-phase (field viscometry) (grey diamond) temperature versus the bubble-free groundmass crystallinity (Φ_c). (B) IDE and field data viscosities versus the bubble-free groundmass crystallinity (Φ_c). Note that the grey field denotes the region of field and laboratory data overlap. Error bars correspond to 2σ crystal content variability of the analyzed SEM images.*

We note that the high-crystal fraction IDE data measured at 1155℃ does not follow the near-exponential prediction of any of the models. Data from this experiment show viscosity fluctuation during the thermal equilibrium plateau of the 1155°C IDE (Fig. 2B), and visual inspection of the crucible post-quenching (Fig. S1.1) highlights that this sample has undergone viscous rupture (*i.e.,* pāhoehoe-'a'a transition, Di Fiore et al., 2021). Suppressing this viscous rupture in experiments at high crystal content may be possible when using a lower shear rate, but would hinder inter-comparison between experimental runs. Lower strain rates would force experimentation into the lower end of deformation regimes and obscure the flow properties (Non-Newtonian) that are experienced from higher strain rate ranges of lava emplacement.

Harris et al. 2025 Author Accepted Manuscript. Earth and Planetary Science Letters
Accepted 12 September 2025: https://doi.org/10.1016/j.epsl.2025.1196

4.2 Integration of Field and Laboratory Viscosity Data

Here, we mapped the rheological behavior of the LH lavas, employing the most robust experimental approach available. This includes full characterization of melt viscosity (Fig. 2A) and, for the first time, the crystallization-induced evolution of apparent viscosity both in equilibrium (IDE, Fig. 2B) and disequilibrium conditions (CDE, Fig. 2C, D), all under near-eruptive reduced atmospheric conditions. All the methods used here encompass conventional techniques for basaltic rheology studies that have been employed for decades but were mostly applied separately until now (*e.g.,* Ryerson et al., 1988; Ishibashi and Sato, 2007; Kolzenburg et al., 2018a; Di Fiore et al., 2024).

The combination of IDEs and CDEs characterizes the viscosities of remelted lava across wide ranges of temperatures, providing a detailed quantification of the lava's two-phase rheology. The true transferability of these data to lava emplacement in nature has remained cryptic because, before now, they were never tied to field viscosities, temperature measurements, and textural characterization of natural lava (Chevrel et al., 2019).

In this study, laboratory and field measurements overlap in crystallinity (Φ_c) and viscosity-temperature space (Figs. 2D, 3, and 4). The lowest field viscosity data (~$10^{2.5}$ Pa s) at the highest measured temperature (1165℃) plot well above the liquid viscosity curve (Fig. 2D). This is expected since the near-vent lava did not erupt as a single-phase liquid and contained ~25 vol.% crystals (from magma chamber or conduit crystalization) (Figs. 3G, 4A; Table 2; Harris et al., 2024a). This observation highlights that viscosity measurements of single-phase melts at super liquidus temperatures, while practical for understanding silicate-melt rheology, are not directly applicable for understanding natural three-phase lava behavior. Additionally, it is well known that basaltic lava flows have an increasing crystallinity and decreasing vesicularity downflow (e.g., Crisp et al, 1994), and this is also the case for LH lavas (Harris et al, 2024a). The LH lavas' crystallinity increased from ~25% to ~50% and vesicularity decreased from 32% to 2% along the flow length (driven through cooling of ~5℃/km; Harris et al., 2024a). Thus, a range of realistic textural characteristics must be considered when investigating natural lava rheology.

IDE data are useful for the investigation of crystallization-induced viscosity changes in two-phase systems (melt+crystals). In the dilute crystal regime ($\Phi_c <$ 40%), we obtain a good agreement in terms of viscosity versus crystal fraction between IDE and field data. However, in the concentrated crystal regime ($\Phi_c =$ 47%), IDEs lead to an underestimate of the field lava viscosity (Fig. 4). This misfit between the IDE and field data is likely due to limitations in the experimental methods where

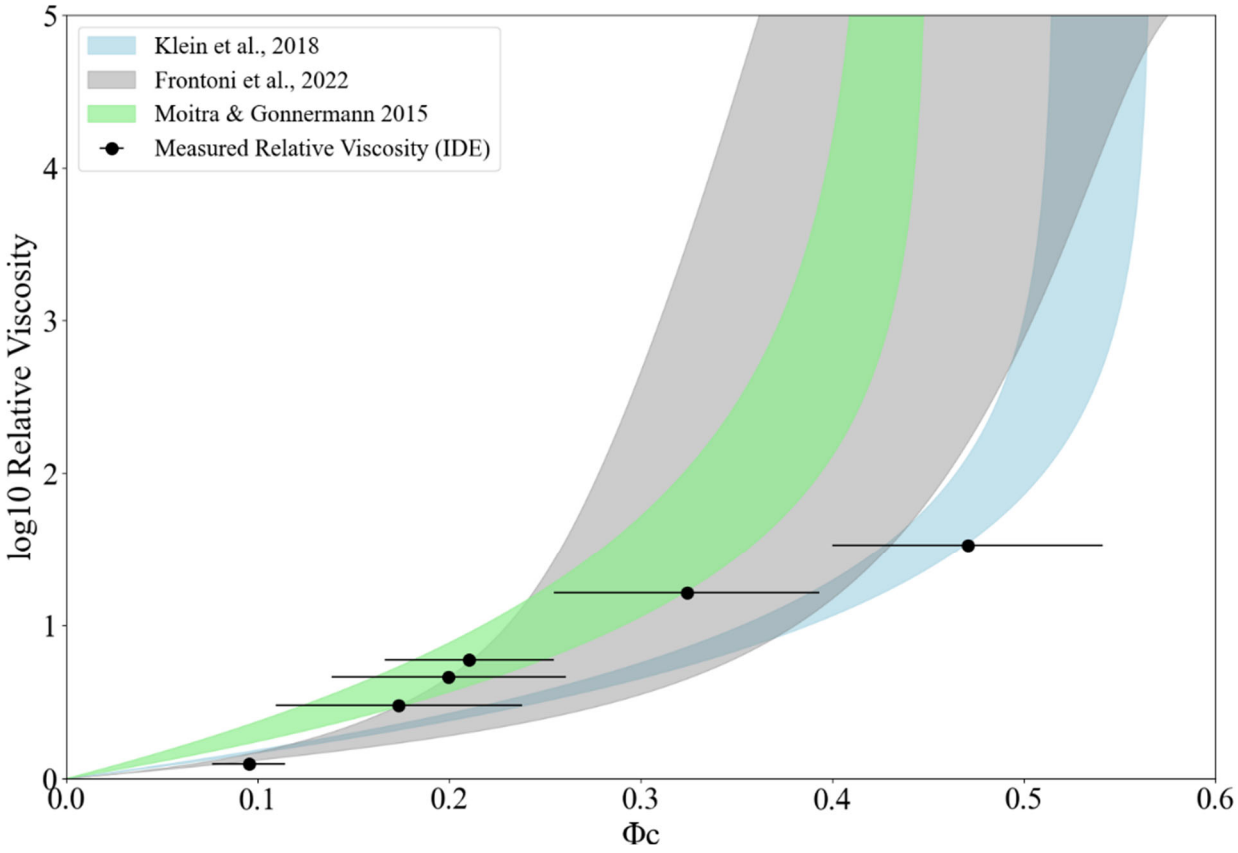

Harris et al. 2025 Author Accepted Manuscript. Earth and Planetary Science Letters
Accepted 12 September 2025: https://doi.org/10.1016/j.epsl.2025.1196

Figure 5: *A Comparison of two-phase IDE relative viscosity with bubble-free crystal fraction (Φ_c) (black circles) with empirical two-phase particle suspension models. The dashed boundaries mark the calculated maximum and minimum viscosities based on textural variations of the quenched IDE material. 2σ x-error bars are shown for IDE Φ_c variability of the analyzed SEM images.*

laboratory concentric-cylinder viscometry induces detachment in the crucible when the sample transitions into the 'a'a regime, while the field data are collected with axial viscometry that is optimized for these transitional to 'a'a lavas (Harris et al., 2024a, 2024b). Therefore, caution must be taken when using IDE data to infer natural lava flow behavior beyond the dilute crystal regime (Φ_c > 40%), especially for the interpretation of the rheology of 'a'a lava.

We find agreement between laboratory CDE and field viscosities across temperatures between 1150 and 1165 ℃, at cooling rates of 0.5 and 1 °C/min (Fig. 2D). The near-exponential increase in field viscosity of 2 orders of magnitude is comparable to the viscosity-temperature profiles recorded in the CDE experiments. Ultimately, the data integration presented here highlights that in the absence of field viscosities, the CDE approach (under fO_2 conditions relevant to nature) can be used to best represent natural lava viscosity/temperature evolution and guide the bounding viscosity range for lava flow models (*e.g.,* Cappello et al., 2016; Chevrel et al., 2018b; Hyman et al., 2022).

4.3 Effect of Bubbles on Lava Viscosity

The natural textures of the LH lavas document bubbles in the high Capillary Number (Ca) regime (*i.e.,* deformable bubbles) (*c.f.,* Harris et al., 2024a), which are expected to reduce the effective viscosity of the material (Llewellin and Manga, 2005; Mader et al., 2013). We model the influence of bubbles in three-phase lava by applying the effective medium theory. For this, the effect of the addition of high-Ca bubbles on the viscosity of the two-phase (crystal + melt) IDE data (which are considered as the effective medium) is evaluated, and we test how well the model can reproduce the measured three-phase field viscosities. Given that none of the two-phase empirical models adequately recover the IDE data (see above; Fig. 5), we use a power law fit for the IDE data, excluding the experiment at 1155 ℃ (see discussion above), to represent the bubble-free effective medium viscosity:

$$(\eta_r = 3.33 \times 10^4 \times \Phi_c^{3.08};\ R^2 = 0.99\ ).$$

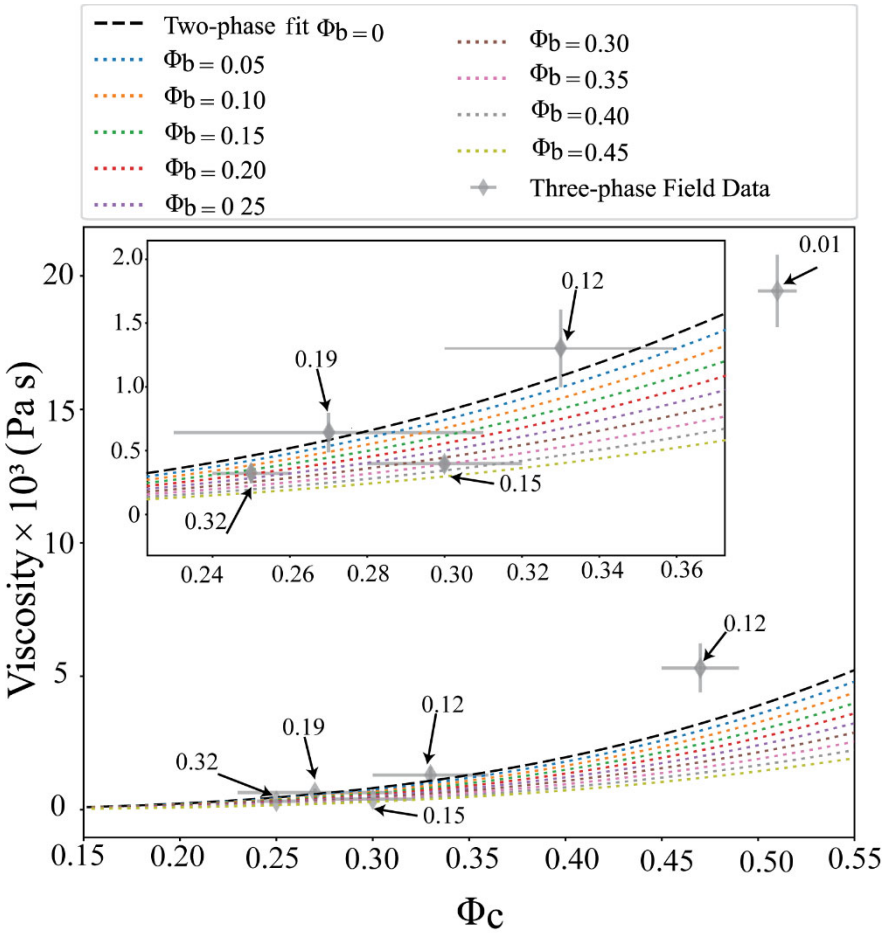

Harris et al. 2025 Author Accepted Manuscript. Earth and Planetary Science Letters
Accepted 12 September 2025: https://doi.org/10.1016/j.epsl.2025.1196

Figure 6: *Modeled effect of adding bubbles (as increasing bubble fraction) to the two-phase IDE laboratory data (Φ_b= 0) using the effective medium theory with the empirical approach by Mader et al. (2013). Plots show the modeled effect in 2-dimensional space, with contours being different Φ_b. The natural three-phase field data are shown in grey diamonds with 2σ error shown for viscosity and groundmass crystallinity, Φ_c of the natural data are labeled for each point, where uncertainties are reported in Table 2. Each field data point is labeled with its Φ_b, also reported in Table 2.*

We model the effect of high Ca bubbles following Mader et al. (2013), who employ a modified equation of Llewellin and Manga (2005). The model predicts that the addition of bubbles causes a viscosity reduction that increases with higher Φ_b (color-contour intervals in Fig. 6), and we use these data for comparison to the measured three-phase field data (Fig. 6 and 7).

The viscosity misfit between results from our effective medium calculation and field measurements is evaluated in a three-dimensional (viscosity, Φ_b, Φ_c) space (Fig. 7). If any part of the field data uncertainty indices boxes touches the model mesh surface, the misfit is deemed 0. If no point of contact is present, then the difference between the closest point of the uncertainty boxes to the model mesh is calculated and reported as the misfit in viscosity at respective Φ_b and Φ_c (Figs. 7B, C).

We find that crystal growth within natural lavas dominates the rheological evolution of lavas during emplacement, and bubbles play a secondary role. Only in samples with high bubble volume fractions (Φ_b ~30%) (*i.e.,* near vent, high temperature, and low viscosity) is the influence of bubble reduction on the effective viscosity in agreement with model predictions (Fig. 6). This suggests that the rheological effect of bubbles needs to be accounted for when modeling near-vent pāhoehoe lavas (*c.f.,* Chevrel et al., 2018a). It remains difficult to constrain a systematic effect of bubbles because pāhoehoe lavas are texturally heterogeneous (Field Sites 1 to 4). However, the viscosity of these pāhoehoe lavas is within a narrow range, and the viscosity variability resulting from bubbles may not have major implications for the results of hazard assessments based on multi-phase-suspension models. These insights are constrained to one single dataset so far, and obtaining more systematic data to integrate the three-phase viscosity of bubbly lavas with bubble-free laboratory data must be done in the future to validate this hypothesis.

The misfit for the model is low for dilute crystal ranges (Φ_c < 0.2-3) and highest for Φ_c > 0.4 and low bubble content $\Phi_b \leq 0.1$. Bubbles do not seem to be the cause of the misfit because the bubble fraction is low and should reduce viscosity instead of the observed increase (Figs. 6,7). Instead, the misfit is likely due to the underestimated two-phase (melt + crystals) viscosity from the IDE data that poorly recovers the measured field-viscosity ranges in the concentrated crystal regime (see above). We do note that these findings are relevant only to the textures of the LH lavas and could be different for more bubble-rich lava, particularly if bubbles are retained in higher volumes (>10%) along the flow fronts. In those scenarios, the effect of bubbles would likely serve to reduce the effective viscosity of the lava beyond the near-vent region of the flow field. There are currently no models or field data for lava that is both governed by creep flow and is bubble-rich, making these conditions an outstanding region for future study.

Ultimately, well-parameterized, three-phase field viscosities in the concentrated crystal regime (Φ_c > 0.4%) are needed to better understand how lava rheology changes across the pāhoehoe-'a'a transition. This morphological change in naturally flowing lavas represents the point where lava viscosity begins to increase exponentially (Harris et al. 2024a), which is important to constrain for accurate flow simulations during hazard assessments. The disagreement between the field data and the suspension model predictions poses an element of uncertainty in evaluating the effect of crystals on the flow behavior of natural lavas. Care should be taken if natural lava texture is used to estimate Φ_{max} within these existing empirical models, because it may result in a large overestimation of viscosity (Harris et al., 2024a; Fig. 8). Conversely, the IDE data are unable to capture the viscosity at high crystal volume fraction because of viscous rupture at shear rates relevant to lava emplacement (Fig. 8), leaving field derived viscometry as the best current method to investigate the viscosity of flowing lavas at high crystal volume.

Harris et al. 2025 Author Accepted Manuscript. Earth and Planetary Science Letters
Accepted 12 September 2025: https://doi.org/10.1016/j.epsl.2025.1196

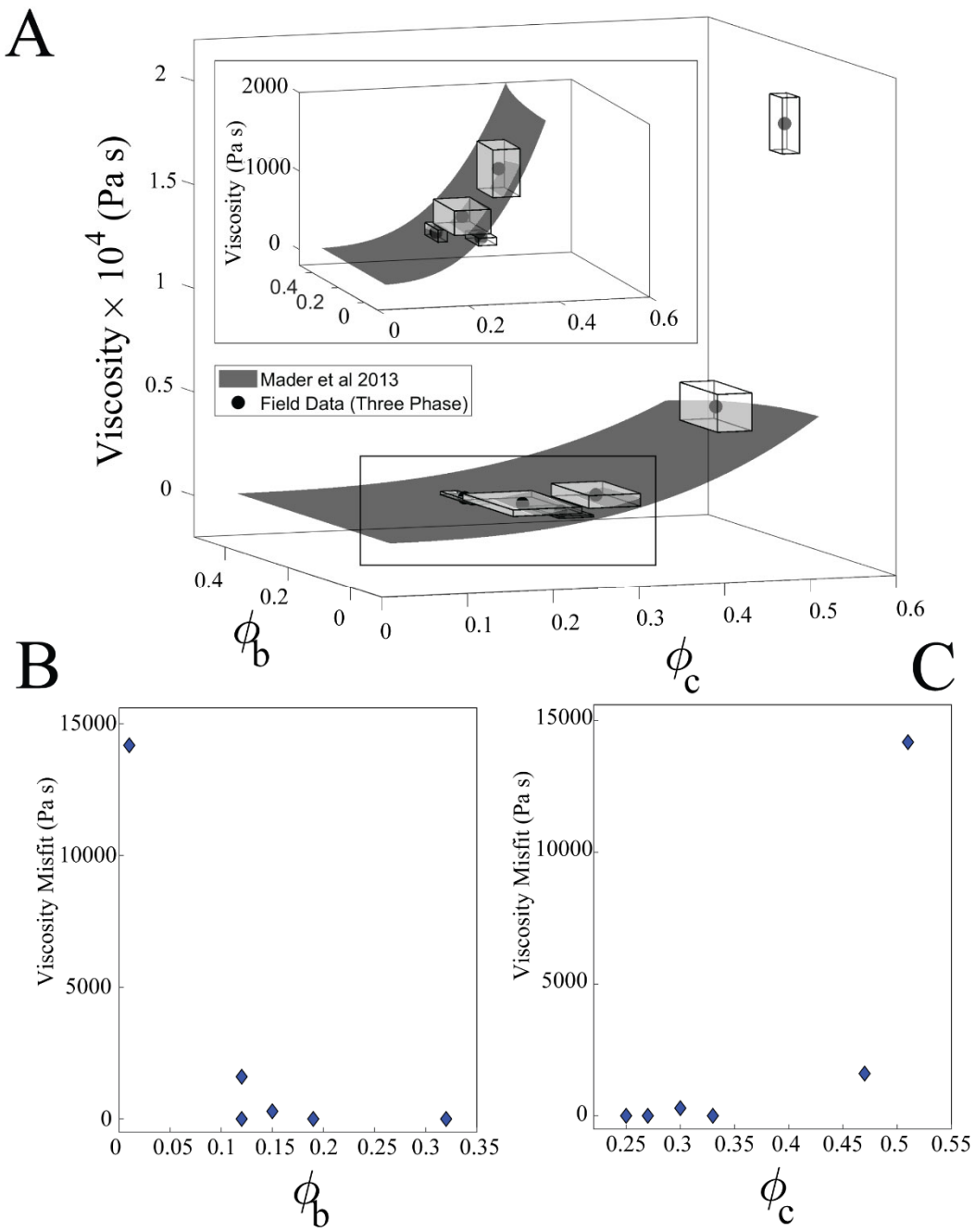

Figure 7: *Comparison of field data with three-phase viscosity calculated from the effective medium approach, with the effect of bubble modeled from Mader et al. (2013). A) Three-dimensional representation of the viscosity calculated from the three-phase effective medium theory, versus Φ_c and Φ_b. The natural three-phase field data are plotted (black dots) with their error indices. B) and C) Calculated viscosity misfits between the empirical three-phase model and the measured three-phase field viscosities as a function of Φ_b (B) and Φ_c (C).*

Harris et al. 2025 Author Accepted Manuscript. Earth and Planetary Science Letters
Accepted 12 September 2025: https://doi.org/10.1016/j.epsl.2025.1196

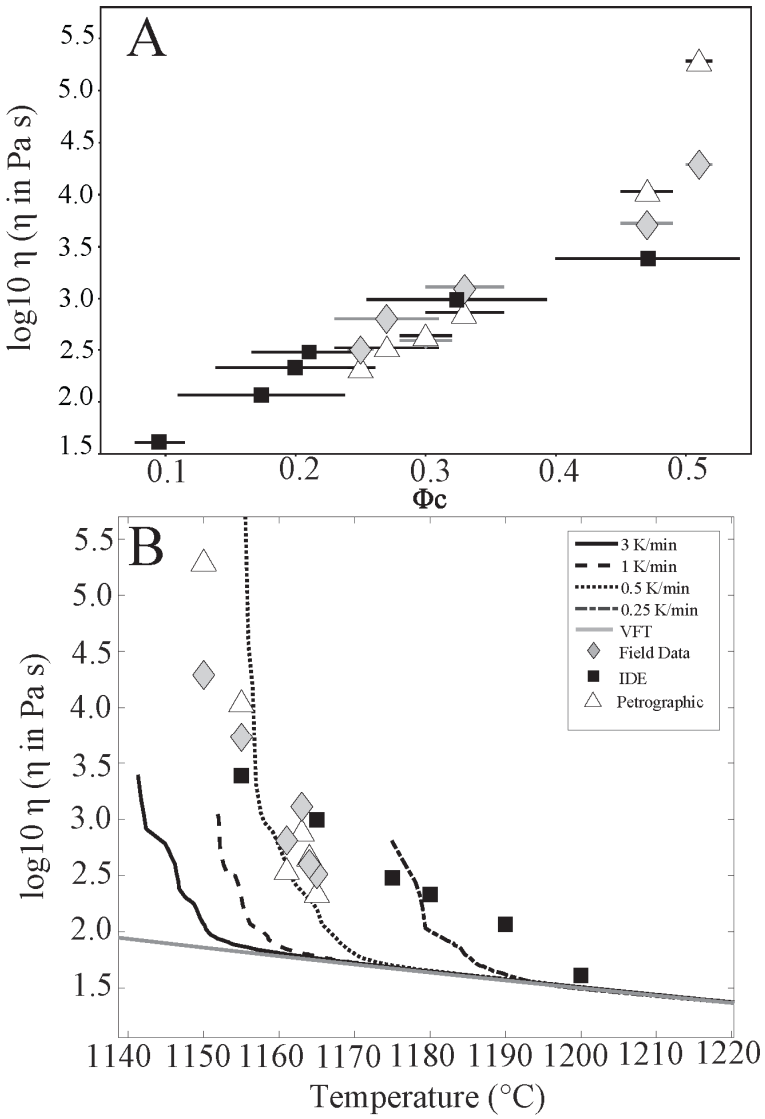

***Figure 8**: A) Plot showing IDE (Black Square), field data (grey diamond), and petrographically derived (white triangle; see Harris et al. 2024a; Table 2) viscosities versus the bubble-free groundmass crystallinity (Φ_c). Error bars correspond to 2σ crystal content variability of the analyzed SEM images. B) Integration of all measurements, including liquid viscosity (VFT fit, grey line), the apparent viscosity of the CDE at varying cooling rates, IDE (black square), field viscosity (grey diamond), and petrographically derived viscosities (white triangle).*

4.4 Implications for Future Lava Rheological Studies

This study presents single (melt), two (melt+crystal), and three-phase (melt+crystal+bubble) viscosity data of lava through the integration of field and laboratory viscometry. This approach provides a comprehensive characterization of the lava's flow properties covering the range of textures, temperatures, and fO2 relevant to naturally flowing lava (Fig. 2). These specific values derive from measurements of the LH lavas, but we identify a series of implications that are transferable to future rheological studies of natural multiphase lava.

1. The data presented here highlights that any meaningful laboratory experimental assessment of flow properties that is relevant and applicable to natural lava emplacement needs to consider both crystallization and fO2. Performing measurements at reduced conditions that are relevant to the emplacement scenarios (i.e., lower than atmospheric fO2) is imperative for experiments because this influences phase dynamics and crystallization kinetics in addition to pure melt viscosity. By doing so, the data presented here show that it is possible to recover within the experiments the crystallinity phase type and abundance of what is naturally occurring. This is essential for future work

Harris et al. 2025 Author Accepted Manuscript. Earth and Planetary Science Letters
Accepted 12 September 2025: https://doi.org/10.1016/j.epsl.2025.1196

that aims to investigate, in particular, the rheology of lavas at concentrated crystallinity (Φc ≥ 40-70%).

2. We find the best agreement between field viscosities and laboratory data to derive from disequilibrium (CDE) experiments. Both datasets document a near-exponential increase over a comparable viscosity-temperature space. This is the first field validation of the assumption that experimental data from laboratory measurements can be used for lava flow modeling. In the absence of in-situ measurements, we recommend that a series of CDE may be used to best represent the viscosity-temperature relationship of naturally evolving lava. A series of CDEs at relevant fO2, temperatures, and shear rates can be conducted within 2-3 days of continuous experimentation and could therefore guide the bounding viscosity range for lava flow models in the early phases of an effusive eruption.

3. Field viscometry is the best available method to obtain the three-phase viscosity of lava, yet this methodology remains underutilized, and available data is sparse. There is an inherent need for continued efforts in this field and to integrate these with laboratory data.

4. There needs to be a revitalized effort to design experiments both on silicate melts and analog materials that contain all three relevant phases (liquid, solid, gas). In particular, there should be a focus on mixtures with bubbles in the high Ca regime (Ca >1) and at crystal contents beyond the dilute limit (Φc ≥ 40%). These are relevant conditions for naturally flowing lava (e.g., basalts), yet are where the current empirical models and experiments (i.e., IDE) break down and either overestimate or underestimate the lava viscosity. Expanded experimentation of three-phase suspensions will help decipher whether the effective medium theory is appropriate in its independent treatment of suspended phases in the concentrated regime. The implementation of the effective medium approach on the LH lavas is only effective in recovering the measured three-phase viscosities up through the dilute crystal suspension regime (Φc < 40%). To date, few analog studies have combined three-phase mixtures to test the validity of the effective medium theory (c.f., Truby et al., 2015; Birnbaum et al., 2021), but these studies were limited to low capillary-number (Ca) rigid bubbles (e.g., Truby et al., 2015) and particle proportions restricted to the dilute regime (Φc ≤ 0.37; e.g., Birnbaum et al., 2021).

5. Studies limited to the super-liquidus viscosity of remelted lava have little applicability to the assessment of eruptive scenarios and cannot be used to indicate the continuation (or not) of an eruption.

5 Summary

This study presents the integration of viscosity data from laboratory-derived single- and two-phase measurements with three-phase data from field measurements on the 2023 Litli-Hrútur eruption in Iceland. The laboratory methods used here recreate natural emplacement conditions as best as possible, such as reduced conditions at log fO2 = −8.7 at eruption temperatures and running equilibrium and disequilibrium experiments across temperatures, cooling, and shear rates relevant to the natural emplacement. We find that the experiments performed within temperatures that match field conditions (1150-1165 ℃) overlap in viscosity (~$10^{2.5}$ to $10^{4.5}$ Pa s) and suggest cooling rates of 0.5-1 ℃/min as most relevant. We document overlapping crystallinity for equilibrium laboratory measurements and natural samples (~20-50%), which enables direct comparison of two-phase (melt+crystal) and three-phase (melt+crystal+bubble) viscosities. We find that bubbles do not reduce the lava viscosity beyond the nearest vent samples (~30% bubble volume) and that crystallinity changes from the dilute to the concentrated regime (>40% crystal volume) are the major drivers in viscosity increase along a naturally flowing lava. This concentrated regime is also where the empirical suspension models, and their use in an effective medium approach, tend to break down in their ability to recover the measured three-phase viscosity of lavas. This must be considered when modeling lava flow hazards, as natural lava might be lower in viscosity than what petrographic approaches calculate and potentially higher in viscosity than what IDEs may indicate. Future experimentation is needed to fully constrain the effects of interacting suspended phases within natural three-phase lavas. Currently, in-situ field viscometry yields the most rapid and accurate determination of multiphase lava.

Harris et al. 2025 Author Accepted Manuscript. Earth and Planetary Science Letters
Accepted 12 September 2025: https://doi.org/10.1016/j.epsl.2025.1196

6. Data Availability Statement

All data that support the findings of this study are available upon the request from the corresponding author.

7. Author Contributions

M.A. Harris, S. Kolzenburg, and M.O. Chevrel conceptualized the study. M.A. Harris and M.O. Chevrel performed field-viscometry. M.A. Harris and S. Kolzenburg conducted laboratory viscometry. All authors participated in data synthesis, processing, and interpretation. All authors contributed to the writing of the article.

8. Funding

Funding was provided by the UB Geohazards Center, NSF EAR RAPID Award No. 2241489, NSF EAR Awards No. 2223098, and 2420723. This is a Laboratory of Excellence ClerVolc contribution no. 717.

9. Acknowledgements

We thank Dr. Thorvaldur Thordarson, Dr. Ármann Höskuldsson, Dr. William Mooreland, and Méline Payet--Clerc of the University of Iceland, and Dr. Karim Kelfoun from University Clermont Auvergne, for their generous support during the field measurements done during the Litli-Hrútur eruption. We thank Kevin Cullinan and Thomas Brachmann of the University at Buffalo Instrument Machine Shop for their work on field instrumentation. We thank Thierry Latchimy and Dr. Ingo Sonder for their help on field viscometry electronics. We are indebted to Travis Parsons for his crucial help with the logistics of assembly, transport, and use of the field and laboratory viscometers. Funding was provided National Science Foundation (NSF) EAR RAPID award no. 2241489, as well as NSF EAR awards no. 2223098 and 2420723.

10. References

Arzilli, F. et al., 2022, Dendritic crystallization in hydrous basaltic magmas controls magma mobility within the Earth's crust: Nature Communications, v. 13, doi:10.1038/s41467-022-30890-8.

Arzilli, F. et al., 2019, Magma fragmentation in highly explosive basaltic eruptions induced by rapid crystallization: Nature Geoscience, v. 12, p. 1023–1028, doi:10.1038/s41561-019-0468-6.

Bamber, E.C. et al., 2025, 3D quantification of nanolites using X-ray ptychography reveals syn-eruptive nanocrystallisation impacts magma rheology: Nature Communications, v. 16, p. 1–15, doi:10.1038/s41467-025-62444-z.

Birnbaum, J., Lev, E., and Llewellin, E.W., 2021, Rheology of three-phase suspensions determined via dam-break experiments: Proceedings of the Royal Society B: Biological Sciences, v. 477, doi:10.1098/rspa.2021.0394.

Cappello, A., Hérault, A., Bilotta, G., Ganci, G., and Del Negro, C., 2016, MAGFLOW: a physics-based model for the dynamics of lava-flow emplacement: Geological Society, London, Special Publications, v. 426, p. 357–373, doi:10.1144/SP426.16.

Cashman, K. V., Thornber, C., and Kauahikaua, J.P., 1999, Cooling and crystallization of lava in open channels, and the transition of Pāhoehoe Lava to 'A'ā: Bulletin of Volcanology, v. 61, p. 306–323, doi:10.1007/s004450050299.

Chevrel, M.O., Platz, T., Hauber, E., Baratoux, D., Lavallée, Y., and Dingwell, D.B., 2013, Lava flow rheology: A comparison of morphological and petrological methods: Earth and Planetary Science Letters, v. 384, p. 109–120, doi:10.1016/j.epsl.2013.09.022.

Chevrel, M.O., Cimarelli, C., DeBiasi, L., Hanson, J.B., Lavallée, Y., Arzilli, F., and Dingwell, D.B., 2015, Viscosity measurements of crystallizing andesite from Tungurahua volcano (Ecuador): Geochemistry Geophysics Geosystems, p. 1–20, doi:10.1002/2014GC005661.

Chevrel, M.O., Harris, A.J.L., James, M.R., Calabrò, L., Gurioli, L., and Pinkerton, H., 2018a, The viscosity of pāhoehoe lava: In situ syn-eruptive measurements from Kilauea, Hawaii: Earth and Planetary Science Letters, v. 493, p. 161–171, doi:10.1016/j.epsl.2018.04.028.

Chevrel, M.O., Harris, A.J.L., Peltier, A., Villeneuve, N., Coppola, D., Gouhier, M., and Drenne, S., 2022, Volcanic crisis management supported by near real-time lava flow hazard assessment at Piton de la Fournaise, La Réunion: Volcanica, v. 5, p. 313–334, doi:10.30909/vol.05.02.313334.

Chevrel, M.O., Labroquère, J., Harris, A.J.L., and Rowland, S.K., 2018b, PyFLOWGO: An open-source platform for simulation of channelized lava thermo-rheological properties: Computers and Geosciences, v. 111, p. 167–180, doi:10.1016/j.cageo.2017.11.009.

Chevrel, M.O., Latchimy, T., Batier, L., Delpoux, R., Harris, M.A., and Kolzenburg, S., 2023, A new portable field rotational viscometer for high-temperature melts: Review of Scientific Instruments, v. 94, doi:https://doi.org/10.1063/5.0160247.

Chevrel, M.O., Pinkerton, H., and Harris, A.J.L., 2019, Measuring the viscosity of lava in the field: A review: Earth-Science Reviews, v. 196, doi:10.1016/j.earscirev.2019.04.024.

Costa, A., Caricchi, L., and Bagdassarov, N., 2009, A model for the rheology of particle-bearing suspensions and partially molten rocks: Geochemistry, Geophysics, Geosystems, v. 10, p. 1–13, doi:10.1029/2008GC002138.

Crisp, J., Cashman, K. V., Bonini, J.A., Hougen, S.B., and Pieri, D.C., 1994, Crystallization history of the 1984 Mauna Loa lava flow: Journal of Geophysical Research: Solid Earth, v. 99, p. 7177–7198, doi:https://doi.org/10.1029/93JB02973.

Deines, P., Nafziger, R.H., Ulmer, G.C., and Woermann, E., 1976, Temperature-oxygen fugacity tables for selected gas mixtures in the system C-H-O at one atmosphere total pressure: Metallurgical Transactions B, v. 7, p. 143, doi:10.1007/bf02652831.

Dingwell, D.B., and Virgo, D., 1987, The effect of oxidation state on the viscosity of melts in the system Na2O-FeO-Fe2O3-SiO2: Geochimica et Cosmochimica Acta, v. 51, p. 195–205, doi:10.1016/0016-7037(87)90231-6.

Di Fiore, F. et al., 2023, Experimental Constraints on the Rheology of Lavas From 2021 Cumbre Vieja Eruption (La Palma, Spain): Geophysical Research Letters, v. 50, doi:10.1029/2022GL100970.

Di Fiore, F., Vona, A., Di Genova, D., Pontesilli, A., Calabrò, L., Mollo, S., Taddeucci, J., Romano, C., and Scarlato, P., 2024, Magma titanium and iron contents dictate crystallization timescales and rheological behaviour in basaltic volcanic systems: Communications Earth and Environment, v. 5, doi:10.1038/s43247-024-01452-1.

Di Fiore, F., Vona, A., Kolzenburg, S., Mollo, S., and Romano, C., 2021, An Extended Rheological Map of Pāhoehoe—'A'ā Transition: Journal of Geophysical Research: Solid Earth, v. 126, p. 1–23, doi:10.1029/2021JB022035.

Fanesi, E. et al., 2025, A review of the differential scanning calorimetry shift–factor approach: Application to Colli Albani melt viscosity and implications for mafic Plinian eruptions: Journal of Volcanology and Geothermal Research, v. 461, p. 108276, doi:10.1016/j.jvolgeores.2025.108276.

Frontoni, A., Costa, A., Vona, A., and Romano, C., 2022, A comprehensive database of crystal-bearing magmas for the calibration of a rheological model: Scientific Data, v. 9, p. 1–12, doi:10.1038/s41597-022-01363-w.

Fulcher, G.S., 1925, Analysis of recent measurements of the viscosity of glasses: Journal of American Ceramic Society, v. 8.

Di Genova, D., Vasseur, J., Hess, K.U., Neuville, D.R., and Dingwell, D.B., 2017, Effect of oxygen fugacity on the glass transition, viscosity and structure of silica- and iron-rich magmatic melts: Journal of Non-Crystalline Solids, v. 470, p. 78–85, doi:10.1016/j.jnoncrysol.2017.05.013.

Giordano, D., Russell, J.K., and Dingwell, D.B., 2008, Viscosity of magmatic liquids: A model: Earth and Planetary Science Letters, v. 271, p. 123–134, doi:10.1016/j.epsl.2008.03.038.

Giuliani, G., Di Genova, D., Di Fiore, F., Mollo, S., Dominijanni, S., Petrone, C.M., Romano, C., and Vona, A., 2025, The rheological evolution of a phonotephritic melt upon variable degrees of carbonate assimilation and deformation regimes: Chemical Geology, p. 122711, doi:https://doi.org/10.1016/j.chemgeo.2025.122711.

Halverson, B.A., and Whittington, A., 2024, From flow to furnace : Low viscosity of three-phase lavas measured at Kīlauea 2018 eruption conditions: p. 1–5, doi:10.1130/G52679.1/7037104/g52679.pdf.

Hamilton, D.L., Burnham, C.W., and Osborn, E.F., 1964, The Solubility of Water and Effects of Oxygen Fugacity and Water Content on Crystallization in Mafic Magmas1: Journal of Petrology, v. 5, p. 21–39, doi:10.1093/petrology/5.1.21.

Harris, A.J.L. et al., 2019, Validation of an integrated satellite-data-driven response to an effusive crisis: The april-may 2018 eruption of piton de la fournaise: Annals of Geophysics, v. 62, doi:10.4401/ag-7972.

Harris, M.A., Chevrel, M.O., Parsons, J.T., Latchimy, T., Thordarson, T., Hoskuldsson, A., Moreland, W.M., Payet—Cerc, M., and Kolzenburg, S., 2024a, Real-time, in situ viscosity mapping of active lava: Geology, v. XX, doi:https://doi.org/10.1130/G52558.1.

Harris, M.A., Kolzenburg, S., Sonder, I., and Chevrel, M.O., 2024b, A new portable penetrometer for measuring the viscosity of active lava: Review of Scientific Instruments, v. 95, p. 65103, doi:10.1063/5.0206776.

Hess, K.U., and Dingwell, D.B., 1996, Viscosities of hydrous leucogranitic melts: a non-Arrhenian model: American Mineralogist, v. 81, p. 1297–1300.

Higgins, M.D., 2000, Measurement of crystal size distributions: American Mineralogist, v. 85, p. 1105–1116, doi:10.2138/am-2000-8-901.

Hyman, D.M.R. et al., 2024, Real-time lava flow forecasting during the 2022 Mauna Loa eruption response: Bulletin of Volcanology, v. 87, doi:10.1007/s00445-024-01783-z.

Hyman, D.M.R., Dietterich, H.R., and Patrick, M.R., 2022, Toward Next-Generation Lava Flow Forecasting: Development of a Fast, Physics-Based Lava Propagation Model: Journal of Geophysical Research: Solid Earth, v. 127, p. 1–27,

doi:10.1029/2022JB024998.

Ishibashi, H., and Sato, H., 2007, Viscosity measurements of subliquidus magmas: Alkali olivine basalt from the Higashi-Matsuura district, Southwest Japan: Journal of Volcanology and Geothermal Research, v. 160, p. 223–238, doi:10.1016/j.jvolgeores.2006.10.001.

Klein, J., Mueller, S.P., and Castro, J.M., 2017, The Influence of Crystal Size Distributions on the Rheology of Magmas: New Insights From Analog Experiments: Geochemistry, Geophysics, Geosystems, v. 18, p. 4055–4073, doi:10.1002/2017GC007114.

Klein, J., Mueller, S.P., Helo, C., Schweitzer, S., Gurioli, L., and Castro, J.M., 2018, An expanded model and application of the combined effect of crystal-size distribution and crystal shape on the relative viscosity of magmas: Journal of Volcanology and Geothermal Research, v. 357, p. 128–133, doi:10.1016/j.jvolgeores.2018.04.018.

Kolzenburg, S., Chevrel, M.O., and Dingwell, D.B., 2022, Magma / Suspension Rheology: Reviews in Mineralogy and Geochemistry, v. 87, p. 639–720, doi:10.2138/rmg.2022.87.14.

Kolzenburg, S., Di Genova, D., Giordano, D., Hess, K.U., and Dingwell, D.B., 2018a, The effect of oxygen fugacity on the rheological evolution of crystallizing basaltic melts: Earth and Planetary Science Letters, v. 487, p. 21–32, doi:10.1016/j.epsl.2018.01.023.

Kolzenburg, S., Giordano, D., Cimarelli, C., and Dingwell, D.B., 2016, In situ thermal characterization of cooling/crystallizing lavas during rheology measurements and implications for lava flow emplacement: Geochimica et Cosmochimica Acta, v. 195, p. 244–258, doi:10.1016/j.gca.2016.09.022.

Kolzenburg, S., Giordano, D., Hess, K.U., and Dingwell, D.B., 2018b, Shear Rate-Dependent Disequilibrium Rheology and Dynamics of Basalt Solidification: Geophysical Research Letters, v. 45, p. 6466–6475, doi:10.1029/2018GL077799.

Kolzenburg, S., Giordano, D., Di Muro, A., and Dingwell, D.B., 2019, Equilibrium viscosity and disequilibrium rheology of a high magnesium basalt from piton de la fournaise volcano, la reunion, indian ocean, France: Annals of Geophysics, v. 62, doi:10.4401/ag-7839.

Kolzenburg, S., Giordano, D., Thordarson, T., Höskuldsson, A., and Dingwell, D.B., 2017, The rheological evolution of the 2014/2015 eruption at Holuhraun, central Iceland: Bulletin of Volcanology, v. 79, doi:10.1007/s00445-017-1128-6.

Kolzenburg, S., Hess, K.-U., Berlo, K., and Dingwell, D.B., 2020, Disequilibrium Rheology and Crystallization Kinetics of Basalts and Implications for the Phlegrean Volcanic District: Frontiers in Earth Science, v. 8, doi:10.3389/feart.2020.00187.

Lejeune, A.M., and Richet, P., 1995, Rheology of crystal-bearing silicate melts: an experimental study at high viscosities: Journal of Geophysical Research, v. 100, p. 4215–4229, doi:10.1029/94JB02985.

Llewellin, E.W., and Manga, M., 2005, Bubble suspension rheology and implications for conduit flow: Journal of Volcanology and Geothermal Research, v. 143, p. 205–217, doi:10.1016/j.jvolgeores.2004.09.018.

Mader, H.M., Llewellin, E.W., and Mueller, S.P., 2013, The rheology of two-phase magmas: A review and analysis: Journal of Volcanology and Geothermal Research, v. 257, p. 135–158, doi:10.1016/j.jvolgeores.2013.02.014.

Markl, G., Marks, M.A.W., and Frost, B.R., 2010, On the Controls of Oxygen Fugacity in the Generation and Crystallization of Peralkaline Melts: Journal of Petrology, v. 51, p. 1831–1847, doi:10.1093/petrology/egq040.

Maron, S.H., and Pierce, P.E., 1956, Application of ree-eyring generalized flow theory to suspensions of spherical particles: Journal of Colloid Science, v. 11, p. 80–95, doi:https://doi.org/10.1016/0095-8522(56)90023-X.

Moitra, P., and Gonnermann, H.M., 2015, Effects of crystal shape- and size-modality on magma rheology: Geochemistry, Geophysics, Geosystems, v. 16, p. 1–26, doi:10.1002/2014GC005554.

Mollo, S., Giacomoni, P.P., Coltorti, M., Ferlito, C., Iezzi, G., and Scarlato, P., 2015, Reconstruction of magmatic variables governing recent Etnean eruptions: Constraints from mineral chemistry and P–T–fO2–H2O modeling: Lithos, v. 212–215, p. 311–320, doi:https://doi.org/10.1016/j.lithos.2014.11.020.

Pedersen, G.B.M., Pfeffer, M.A., Barsotti, S., Tarquini, S., De'michieli Vitturi, M., Óladóttir, B.A., and Prastarson, R.H., 2023, Lava flow hazard modeling during the 2021 Fagradalsfjall eruption, Iceland: applications of MrLavaLoba: Natural Hazards and Earth System Sciences, v. 23, p. 3147–3168, doi:10.5194/nhess-23-3147-2023.

Phan-Thien, N., and Pham, D.C., 1997, Differential multiphase models for polydispersed suspensions and particulate solids: Journal of Non-Newtonian Fluid Mechanics, v. 72, p. 305–318, doi:10.1016/S0377-0257(97)90002-1.

Robert, B., Harris, A., Gurioli, L., Médard, E., Sehlke, A., and Whittington, A., 2014, Textural and rheological evolution of basalt flowing down a lava channel: Bulletin of Volcanology, v. 76, p. 1–21, doi:10.1007/s00445-014-0824-8.

Russell, J.K., Giordano, D., and Dingwell, D.B., 2003, High-temperature limits on viscosity of non-

Arrhenian silicate melts: American Mineralogist, v. 88, p. 1390–1394, doi:10.2138/am-2003-8-924.

Ryerson, F.J., Weed, H.C., and Piwinskii, A.J., 1988, Rheology of subliquidus magmas: 1. Picritic compositions: Journal of Geophysical Research: Solid Earth, v. 93, p. 3421–3436, doi:https://doi.org/10.1029/JB093iB04p03421.

Sato, M., 1978, Oxygen fugacity of basaltic magmas and the role of gas-forming elements: Geophysical Research Letters, v. 5, p. 447–449, doi:https://doi.org/10.1029/GL005i006p00447.

Schneider, C.A., Rasband, W.S., and Eliceiri, K.W., 2012, NIH Image to ImageJ: 25 years of image analysis: Nature Methods, v. 9, p. 671–675, doi:10.1038/nmeth.2089.

Truby, J.M., Mueller, S.P., Llewellin, E.W., and Mader, H.M., 2015, The rheology of three-phase suspensions at low bubble capillary number: Proceedings of the Royal Society A: Mathematical, Physical and Engineering Sciences, v. 471, doi:10.1098/rspa.2014.0557.

Vogel, D.H., 1921, Temperaturabhängigkeitsgesetz der Viskosität von Flüssigkeiten: Physikalische Zeitschrift, v. 22, p. 645.

Vona, A., Di Piazza, A., Nicotra, E., Romano, C., Viccaro, M., and Giordano, G., 2017, The complex rheology of megacryst-rich magmas: The case of the mugearitic “cicirara” lavas of Mt. Etna volcano: Chemical Geology, v. 458, p. 48–67, doi:10.1016/j.chemgeo.2017.03.029.

Vona, A., Romano, C., Dingwell, D.B., and Giordano, D., 2011, The rheology of crystal-bearing basaltic magmas from Stromboli and Etna: Geochimica et Cosmochimica Acta, v. 75, p. 3214–3236, doi:10.1016/j.gca.2011.03.031.

Webb, S.L., 2021, Viscosity of evolving magmas: a case study of the Glass House Mountains, Australia: Bulletin of Volcanology, v. 83, doi:10.1007/s00445-021-01495-8.

Willhite, L.N. et al., 2024, Oxygen Fugacity of Global Ocean Island Basalts: Geochemistry, Geophysics, Geosystems, v. 25, p. 1–20, doi:10.1029/2023GC011249.